

PHOTOMASK

BACUS—The international technical group of SPIE dedicated to the advancement of photomask technology.

BACUS

N • E • W • S

OCTOBER 2021
VOLUME 37, ISSUE 10

AL21

Measuring EUV mask 3D effects with hyperspectral Zernike phase contrast

Stuart Sherwin, Laura Waller, and Andrew Neureuther, University of California Berkeley, Department of Electrical Engineering and Computer Science, Berkeley, USA

Ryan Miyakawa, Markus Benk, and Patrick Naulleau, Center for X-Ray Optics, Lawrence Berkeley National Laboratory, Berkeley, USA

ABSTRACT

Achieving the ultimate resolution limit of EUV lithography is greatly impeded by the 3D photomask geometry, including an absorber whose thickness is comparable to the minimum lateral dimensions of the pattern, and a reflection plane a similar depth beneath the surface of the multilayer mirror. Rigorous simulations have shown that these effects can in theory be mitigated by adopting a thinner absorber and a multilayer with a reflection plane closer to the surface. But regardless of how rigorously the design is optimized, there is clearly a need to experimentally confirm that the as-built photomask conforms to the simulation's predicted complex electric field. This experimental confirmation is difficult because only the field's intensity is directly observable. One promising approach to unambiguously make this measurement is Zernike phase contrast imaging, which determines the complex electric field from intensity images acquired from a single illumination condition with different phase shifts on the 0 order. In this work we present an extension to a hyperspectral version of the technique. By varying the wavelength, we are able to empirically observe the complicated interaction between absorber, multilayer, pattern, and illumination. We performed an experimental demonstration of the technique on a patterned EUV mask with 60nm TaN absorber using specially fabricated zone plates on the SHARP EUV microscope at the Center for X-Ray Optics. Our results demonstrate the sensitivity of hZPC to both the Fresnel reflectance as well as more subtle 3D effects also observed in rigorous simulations.

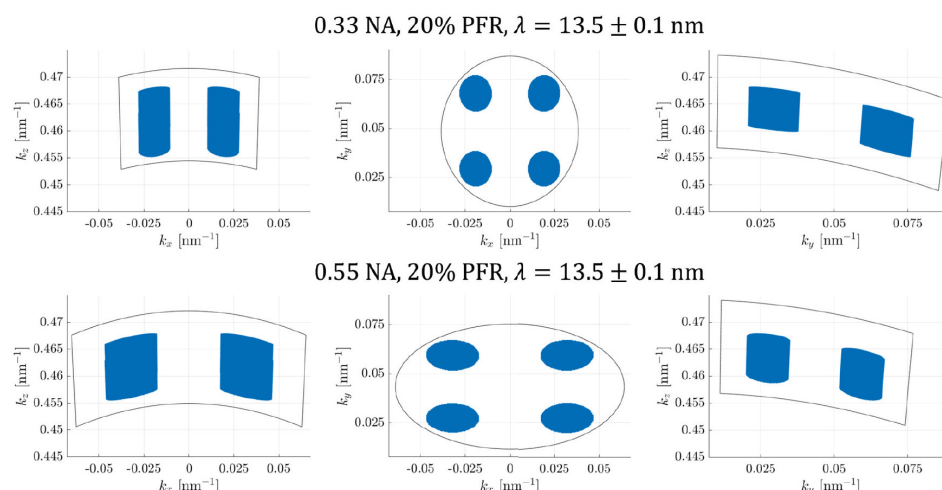


Figure 1. 3D illumination The illumination incident on the mask contains mutually incoherent plane waves with a range of 2D angles as well as a range of wavelengths. Here we show a 3D k -space visualization of quad illumination with a 20% PFR (Pupil Fill Ratio), and a source bandwidth of $\pm 0.1\text{nm}$.

TAKE A LOOK
INSIDE:

INDUSTRY BRIEFS
—see page 12

CALENDAR
For a list of meetings
—see page 13

SPIE.

EDITORIAL

The Phoenix rising from the ashes...

Andy Wall, HOYA Corporation

Early in 2020 I wrote a study on the impact of COVID-19 on the semiconductor industry, forecasting the "new normal" in which we will live and work post pandemic. I was reviewing the accuracy of these predictions recently, which varied from spot-on, to completely insane with hindsight, but that is not a topic for today's editorial. I was reminded of this work in relation to the annual SPIE Photomask Technology + EUVL conference. At the time of writing, the conference is imminent, but by the time you read this it will hopefully have gone ahead with great success. The conference is to be held in a virtual format for the second year running. Yes, virtual again. It's easy to focus on the negative aspect of the pandemic forcing a conference to be virtual, but by doing so we risk missing the fundamental change occurring in the world that is positive for our industry post pandemic.

My new normal predictions considered the shift to remote working, but assumed that when the pandemic is over a large portion of those workers would return to an office. Maybe the pandemic has gone on longer than expected or my vision was not far reaching enough, but it looks increasingly likely that a large portion of the workforce will adopt hybrid or home-working models. Similarly, future in-person conferences will likely continue to include virtual elements to allow remote participation, and so the need for improved remote collaboration tools remains.

Video conferencing and remote collaboration became a necessary evil of the past 18 months. We have become used to staring at a screen of tiled images of our co-workers with hastily combed hair and maybe a sweater pulled over their sleeping attire. Many of us find little enjoyment in a video conference call, but the format may soon change. On 19 August Facebook announced their new technology, Horizon Workrooms (<https://about.fb.com/news/2021/08/introducing-horizon-workrooms-remote-collaboration-reimagined>) which uses VR headsets to gather the meeting participants as avatars inside a simulated room. The technology has traditionally been used for gaming and allows the user to create their own avatar, the image of which will attend the meeting and will mirror gestures that the real-life participant makes. The meeting room can be customized, such as a large conference table, small discussion table, or a university-style lecture theater to attend the next virtual conference. Facebook isn't the only company redesigning virtual meetings; Spatial (<https://spatial.io>) is hosting holographic-style avatars in virtual meeting rooms, and Google's Project Starline allows interaction between 3D images via a custom screen (<https://blog.google/technology/research/project-starline>).

Is this innovation a realistic replacement for the current video-conferencing solutions? In the short term, probably not. The barrier to entry is high as it requires expensive headsets or equipment to implement, and getting multigenerational workforces onboard with this type of dramatic transformation is difficult. The ability to create your avatar's appearance may also inhibit collaboration as you can't see the actual person that you are talking to, not to mention the avatar may look nothing like the real person controlling it. However, it is the trend that is important, with the need to reinvent the digital workspace being accelerated by the pandemic towards the new normal. Long-term, this type of disruptive technology will change the face of video conferencing.

There are many examples of accelerated technology trends as a result of the pandemic that will change our activity in the long-term: consumer habits changed to reduce foot traffic at stores and increase the use of online shopping models; it is now faster and easier to order your coffee via an app on your smartphone than it is to queue in the store and talk to the barista; and schools have adopted online learning for specific topics after they returned to in-person teaching, using applications developed during at-home schooling. Many school children are now being provided with notebooks for the school year to run those applications, providing a long-term boost to the PC market post pandemic, while the social trend towards less human interaction and an expectation of instant gratification has increased the use of applications that drive demand for smartphones, servers, and cloud solutions to name just a few.

COVID-19 has changed our actions and expectations and has pushed us to implement faster change towards the new normal, and as a result we see increased long-term demand for semiconductors. The negative impact of COVID-19 endures, but we should also look for the Phoenix rising from the ashes and recognize and embrace the future trends that will drive our industry. Hopefully next year we can meet in person at the 2022 SPIE Photomask Technology + EUVL Conference, but if the travel restrictions and variants endure, then at least our avatars will be able to meet and discuss the latest and greatest technology for photomasks. In case you don't recognize my avatar, I'll be the young man with a Thor-like physique wearing board shorts and a Hawaiian shirt.



N • E • W • S

BACUS News is published monthly by SPIE for BACUS, the international technical group of SPIE dedicated to the advancement of photomask technology.

Managing Editor/Graphics Linda DeLano
SPIE Sales Representative, Exhibitions, and Sponsorships
Melissa Valum

BACUS Technical Group Manager Tim Lamkins

■ 2021 BACUS Steering Committee ■

President

Emily E. Gallagher, *imec*.

Vice-President

Kent Nakagawa, *Toppa Photomasks, Inc.*

Secretary

Jed Rankin, *GLOBALFOUNDRIES Inc.*

Newsletter Editor

Artur Balasinski, *Infineon Technologies*

2022 Photomask + Technology Conference Chairs

Bryan S. Kasproicz, *HOYA*

Ted Liang, *Intel Corp.*

Members at Large

Frank E. Abboud, *Intel Corp.*

Uwe F. W. Behringer, *UBC Microelectronics*

Peter D. Buck, *Mentor Graphics Corp.*

Brian Cha, *Samsung Electronics Co., Ltd.*

Aki Fujimura, *DS2, Inc.*

Jon Haines, *Micron Technology Inc.*

Naoya Hayashi, *Dai Nippon Printing Co., Ltd.*

Henry Kamberian, *Photronics, Inc.*

Bryan S. Kasproicz, *HOYA*

Romain J. Lallement, *IBM Research*

Jan Hendrik Peters, *bmbg consult*

Abbas Rastegar, *Applied Materials*

Douglas J. Resnick, *Canon Nanotechnologies, Inc.*

Thomas Scheruebl, *Carl Zeiss SMT GmbH*

Ray Shi, *KLA Corp.*

Thomas Struck, *Infineon Technologies AG*

Bala Thumma, *Synopsys, Inc.*

Anthony Vacca, *Automated Visual Inspection*

Vidya Vaenkatesan, *ASML Netherlands BV*

Andy Wall, *HOYA*

Michael Watt, *Shin-Etsu MicroSi Inc.*

Larry Zurbrick, *Keysight Technologies, Inc.*

SPIE.

P.O. Box 10, Bellingham, WA 98227-0010 USA

Tel: +1 360 676 3290

Fax: +1 360 647 1445

SPIE.org

help@spie.org

©2021

All rights reserved.

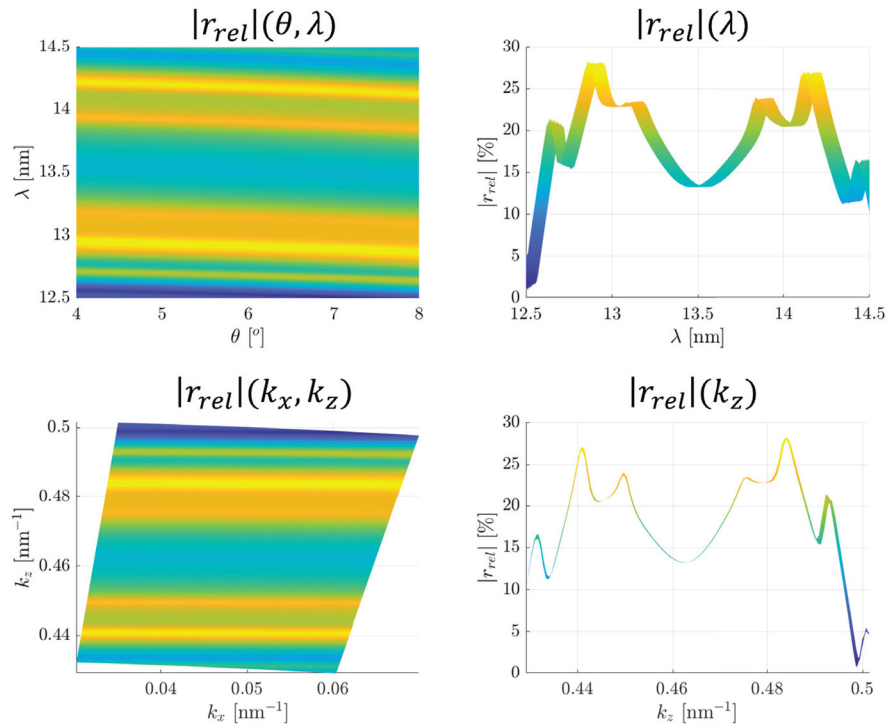


Figure 2. **Fresnel reflectance vs k_z** The Fresnel reflectance, while it depends on both wavelength and angle, is approximately a function of k_z due to planar symmetry. Here we plot the ratio of absorber over multilayer reflectance, as a function of wavelength and angle (top), and as a function of k -vector (bottom).

Introduction

Achieving the ultimate resolution limit of EUV lithography is greatly impeded by the 3D photomask geometry, including an absorber whose thickness is comparable to the minimum lateral dimensions of the pattern, and a reflection plane a similar depth beneath the surface of the multilayer mirror.¹⁻⁴ While these effects can be mitigated by adopting a thinner absorber¹ and a multilayer with a reflection plane closer to the surface,^{3,4} ultimately these designs are optimized by rigorous simulations such as Rigorous Coupled Wave Analysis (RCWA), meaning they are fundamentally limited by the accuracy of the inputs to the RCWA simulation. Therefore bringing these absorber and multilayer designs from simulation to reality might be greatly aided by the ability to experimentally confirm (or calibrate) the predictions of RCWA, to precisely characterize and compensate 3D scattering effects to create a high-quality image at the minimum feature size. The impact of 3D effects will become most severe for printing low- k_l patterns, due to several interlocking problems: the larger source divergence required to maximize resolution will necessitate simultaneously including source points from opposite ends of the pupil, for which both the Fresnel reflectance and shadowing are markedly different; furthermore, the smaller features on the mask will increase the divergence of diffraction orders during reflection, which may require optimizing the phase and/or amplitude response of the multilayer, including angles far beyond the maximum angle of incidence.

But separate from questions of how to mitigate mask 3D effects by optimizing the source, pattern, absorber, and multilayer is the fundamental question of how to measure mask 3D effects. In this work, mask 3D effects are split into two categories: the simpler Fresnel 3D effects and the more general rigorous 3D effects. Both describe mathematical deviations of the scattered electric field from a thin-mask scattering model, with Fresnel 3D effects simply making the multilayer and absorber reflectance functions of the illumination wave vector (representing bulk changes in the Fresnel reflectance) whereas rigorous 3D effects describe any more complicated relationship between illumination, pattern, and scattering. Fresnel 3D effects can in principle be determined from only measurements of bulk multilayer and absorber reflectance, while rigorous 3D effects can only be

measured by recovering the amplitude and phase of all scattered waves from a certain pattern under coherent illumination, which amounts to a spatially resolved measurement of the complex electric field.

We have previously proposed measuring precisely this spatially resolved complex electric field from a given pattern under plane-wave illumination by acquiring multiple images of a feature with a single illumination angle but multiple different imaging transfer functions, and subsequently reconstructing the complex field computationally, where we found that a particularly promising approach for unambiguously determining the complex field was by using a series of Zernike phase contrast zone-plates as our coding elements, which allow us to measure intensity images with different phase shifts on the 0 order.⁵ In this work, we extend our past Zernike phase contrast (ZPC) measurements to also include a scan of illumination wavelength, therefore calling the new technique hyperspectral Zernike phase contrast (hZPC). We present our experimental hZPC measurements of a patterned EUV mask (60nm TaN absorber, standard 40 bilayer Mo-Si multilayer) performed on the SHARP EUV microscope at the Center for X-Ray Optics. The feature in question is a 3:1 line-space pattern with 140nm pitch (560nm on mask) in the horizontal (shadowing) orientation. We measured the feature using a set of 6 zone plates over a range of wavelengths, and then computationally recovered the arbitrary complex diffraction orders for each illumination condition independently, which revealed systematic changes in the electric field as a function of space and wavelength. This trend clearly shows Fresnel 3D effects, where the average electric field in the absorber and multilayer regions of the hZPC reconstruction track closely with the respective Fresnel coefficients determined by reflectometry.⁶ This agreement with reflectometry is a promising validation of the phase recovered from hZPC, but far from the limits of its capabilities. To this end we further demonstrate that hZPC can also measure rigorous 3D effects, or arbitrary variation of the scattered orders, by comparing our experimental reconstruction against a rigorous coupled-wave analysis (RCWA) simulation. While the simulation and experiment are not identical, the simulation contains an idealized geometry which is only qualitatively accurate; so, while acknowledging the differences, we point out the

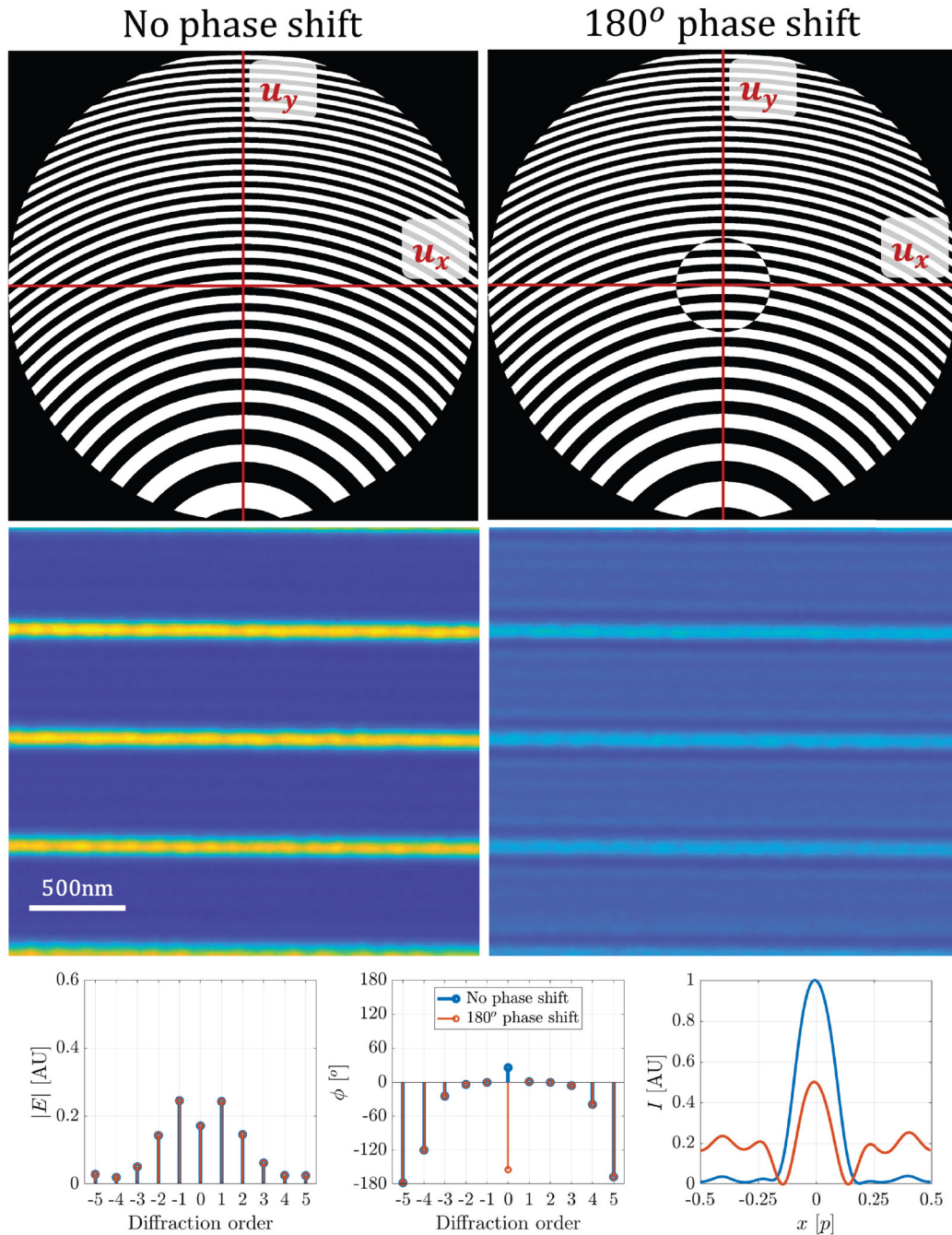


Figure 3. Zernike Phase Contrast (ZPC) Here we demonstrate the overall ZPC technique, where we use a zone plate with a central phase shifted region. The left has no phase shift, and the right has a 180° phase shift. We then show an example of raw data acquired with each zone plate, where we can clearly see differences in contrast for the two images, with the 180° phase shift approximately equalizing the contrast between multilayer and absorber. Finally we show how this difference of contrast arises by phase shifting the 0 order; the amplitude of all orders is the same, as is the phase of all orders but the 0 order, and yet we see a large change in contrast across the entire image.

promising similarities of the hyperspectral diffraction patterns. One of the most striking features that we clearly observe in both simulation and experiment is the asymmetry between positive and negative diffraction orders, which increases for higher order diffraction, a clear indication of shadowing. Shadowing cannot be described by a Fresnel thin-mask scattering model, and depends on interactions between absorber, multilayer, pattern, and illumination. This suggests the vital role that this method can fill in experimentally probing physical effects which were previously accessible only through simulation.

In Section 1 we describe the physical models for illumination and scattering. In Section 2 we describe our experimental methods for Zernike Phase Contrast (ZPC) and hyperspectral ZPC (hZPC). In Section 3 we describe our computational methods for phase retrieval, as well as for making the reflectometry thin-film model compatible with Rigorous Coupled-Wave Analysis (RCWA). And finally in Section 4 we present the results of our hZPC reconstruction and compare against the Fresnel thin-mask and RCWA predictions.

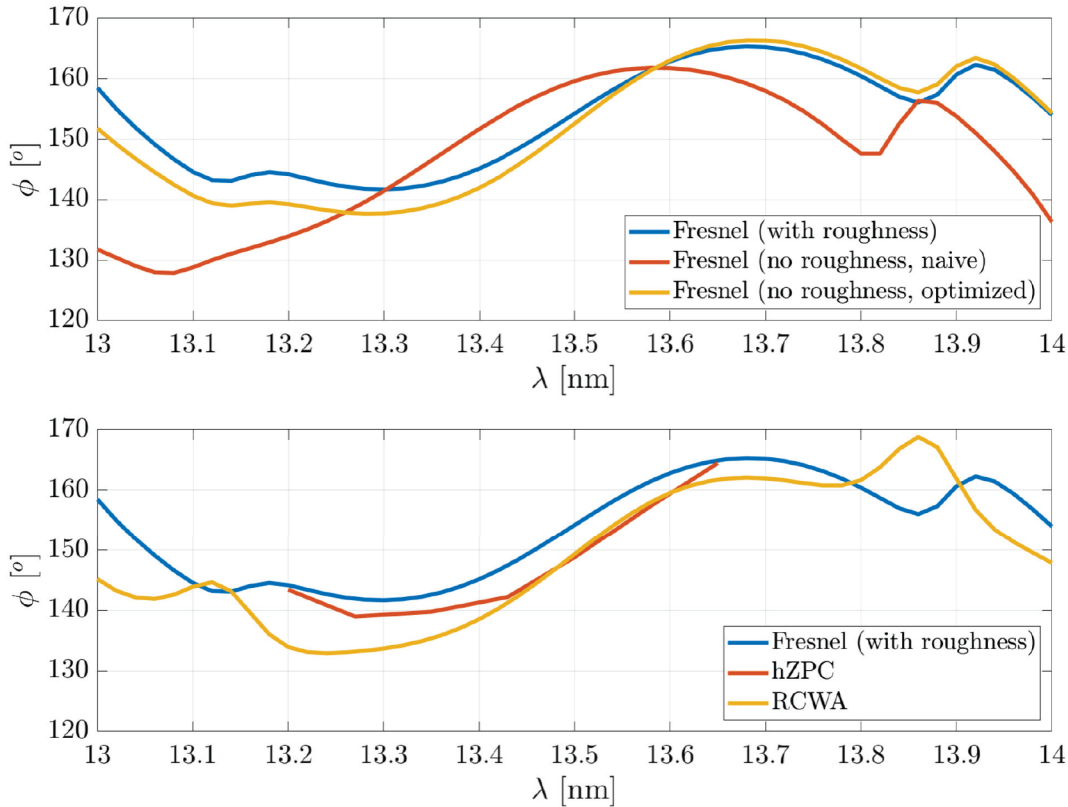


Figure 4. **Fresnel phase** We plot the relative phase (absorber phase minus multilayer phase) as a function of wavelength for different cases. The top plot demonstrates the importance of our optimization procedure to remove roughness, where the optimization allows us to create a roughness-free model whose phase is much closer to the original model than if we were to simply set roughness to 0. The bottom plot compares the Fresnel relative phase to the image-based relative phase (average absorber phase minus average multilayer phase) from hZPC and RCWA.

1. Physical Models

1.1 Imaging with 3D illumination

EUV illumination incident on the mask contains a distribution of mutually incoherent plane waves, with a range of angles set by the source shape and a range of wavelengths set by the light's source spectrum and spectral response of each multilayer mirror coating in the system. Figure 1 shows how the presence of multiple wavelengths requires a 3D description of the illumination. This could either be two angular dimensions plus wavelength, or alternatively the three components of the wave vector (k_x, k_y, k_z). We adopt the latter approach in Figure 1, where we can see that the spread of just ± 0.1 nm in wavelength leads to a large range of k_z values for each illumination angle. One reason to make this change of coordinates is that the reflectance of both multilayer and absorber are essentially independent of k_x and k_y , and depend almost exclusively on k_z over this range of angles and wavelengths. This is illustrated in Figure 2, which shows the relative Fresnel coefficient $r_{rel} = \frac{r_{Abs}}{r_{ML}}$, which is the absorber coefficient divided by the multilayer. This figure clearly shows that whereas the reflectance does have some noticeable variation orthogonal to λ , it has almost no variation orthogonal to k_z . Therefore, referring back to Figure 1, we can see that different source points will have different values of Fresnel reflectance, both in the y direction, where the offset chief ray makes the variation asymmetric, as well as in the x direction where the variation is at least symmetric. Each source point produces a different scattered field, which are all imaged independently and summed incoherently in the final image. If the mask were purely 2D, then it would be possible to ignore how scattering varies as a function of illumination wave vector; however, once we consider the true 3D geometry of the mask, this is no longer the case.

1.2 Thin-mask scattering

The first scattering model we introduce is the thin-mask model, which reduces scattering to a 2D function.⁷ For a binary mask, the scattering function $S(f_x, f_y)$ becomes just the Fourier transform of the pattern $P(x, y)$:

$$P(x, y) = \begin{cases} 1, & (x, y) \in \text{pattern} \\ 0, & \text{otherwise} \end{cases}; \quad S(f_x, f_y) = \mathcal{F}\{P(x, y)\}.$$

If the absorber is not perfectly attenuating, but instead “leaky,” we may introduce coefficients to scale the multilayer (r_{ML}) and absorber (r_{Abs}), but otherwise keep the same model:

$$S(f_x, f_y) = \mathcal{F}\{r_{ML}P(x, y) + r_{Abs}[1 - P(x, y)]\}.$$

This latter model is sufficient to describe 2D scattering for an absorber with arbitrary attenuation and phase, but is limited by neglecting the effects discussed in the next two sections.

1.3 Fresnel thin-mask scattering

A simple modification that we can make to the thin-mask scattering model to begin accounting for 3D scattering would be to keep the same 2D spatial dependence for absorber and multilayer, but to make the coefficients r_{ML} and r_{Abs} depend on illumination. If we use the Fresnel reflectance for these coefficients, this model can easily be computed so long as a physical model of multilayer and absorber is known; for example in this work we use a physical model that was determined by reflectometry on the same mask.⁶ Because the Fresnel reflectance is calculated from a series of flat layers, it does not cause scattering in k_x or k_y , but only in k_z ; it also depends indirectly on the wavelength because the refractive indices of layers in the stack are functions of wavelength. However, as shown in Figure 2, over the range relevant to EUV lithography

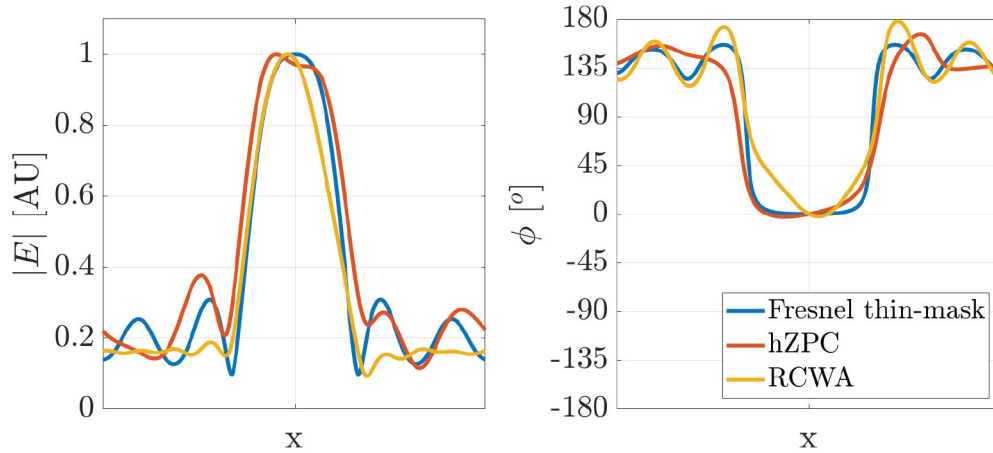


Figure 5. $E(x)$ Electric field as a function of position, for Fresnel thin mask (reflectometry model) ZPC (experiment) and RCWA (roughness-free reflectometry model). Both ZPC and RCWA show asymmetry in amplitude and phase characteristic of shadowing, but the specific deviations from the Fresnel thin-mask model differ.

the dependence on wavelength is much smaller than the dependence on k_x , so we can approximately say $r(k_x, k_y, k_z) \approx r(k_z)$ for both absorber and multilayer coefficients. This reduces the scattering function to a function of 3 dimensions:

$$S(f_x, f_y; k_z) = \mathcal{F}\{r_{ML}(k_z)P(x, y) + r_{Abs}(k_z)[1 - P(x, y)]\}.$$

What this says is that different source points will not experience the same attenuation and phase shift upon reflection, and furthermore that for a given shift in angle there is an equivalent shift in wavelength so long as $k_z = 2\pi \cos \theta / \lambda$ remains constant. As shown in Figure 1, the offset chief ray means that source points with $u_y < 0$ will be closer to normal incidence and $u_y > 0$ will be more oblique, which makes k_z a decreasing function of u_y . On the other hand because the chief ray is centered in the x direction, k_x is a decreasing function of $|u_x|$ (and an even function of u_y).

So ultimately the Fresnel thin-mask model characterizes mask 3D effects that arise from the Fresnel coefficients of multilayer and absorber being functions of illumination wavelength and angle. This already has implications for mask design, such as suggesting that the optimal mask design would likely be source-dependent regardless of the features being printed. However, it fails to capture the full generality of 3D scattering, necessitating a more rigorous approach.

1.4 Rigorous scattering

The most general description of scattering can be obtained from a rigorous simulation such as rigorous coupled wave analysis (RCWA) or finite difference time domain (FDTD). This calculation takes in a 3D refractive index distribution and an illumination wave, and outputs the complex scattered field at a specified output plane. This calculation is generally performed for both TE and TM polarizations, which we neglect in this work; all rigorous results presented are based on TE polarization. If we assume a geometry that is periodic in x and y , with pitch p_x in x and p_y in y , then we can fully specify the electric field in terms of its Fourier expansion into plane waves that are integer harmonics of the fundamental frequencies in x and y .⁷ We index the spatial frequencies by $m, n \in \mathbb{Z}$, where the coefficient for spatial frequency $(m/p_x, n/p_y)$ is $a_{m,n}$:

$$S(f_x, f_y) = \sum_{m,n} a_{m,n} \delta(m/p_x, n/p_y).$$

This expression is valid for a single illumination condition, so in general we need to also allow the coefficients $a_{m,n}$ to vary as functions of (k_x, k_y, k_z) :

$$S(f_x, f_y; k_x, k_y, k_z) = \sum_{m,n} a_{m,n}(k_x, k_y, k_z) \delta(m/p_x, n/p_y).$$

It is this expression rather than the two previous approximations that truly describes scattering for each source point. Generally it has been accessible via simulation, but experimental characterization has been more difficult. In this work though, we present evidence that our proposed Zernike phase contrast (ZPC) method can indeed experimentally

measure a set of complex Fourier coefficients for a periodic feature, and furthermore that with the extension to hyperspectral Zernike phase contrast (hZPC) we can even begin to construct a higher dimensional representation of the scattering function, including arbitrary spatial and illumination dependence.

2. Experimental Methods

2.1 Zernike phase contrast (ZPC)

The key to our technique for measuring the scattered amplitude and phase under a given illumination condition is to measure images taken under the same illumination conditions, but with different imaging transfer functions. To this end we have a set of 6 ZPC zone plates, which each has a 6° chief-ray and 0.55/4 NA, but in the center of each zone plate there is a phase shifted region with a unique phase shift. The phase shifts range from 0° to 300° in steps of 60° . We must always illuminate with a plane-wave aligned with the chief-ray, such that the forward-scattered light (0 orders diffraction) passes through the phase shift. On the other hand light scattered away from the 0 order will pass through the outer part of the zone plate and be imaged with no phase shift. Figure 3 shows two examples of ZPC imaging with a 0° and 180° phase shift, clearly demonstrating how the order phase shift greatly impacts the image contrast by creating either constructive or destructive interference of the scattered light with the background. In addition to the different phase shifts, we also acquire a focal stack for each zone plate, both to account for focus alignment and to increase the number of different transfer functions with which we image the mask.

2.2 Hyperspectral Zernike phase contrast (hZPC)

Experimentally the hZPC measurement is identical to the original ZPC measurement, except that in addition to scanning the 0 order phase shift and the focus, we also scan the illumination wavelength. Note that we must offset the focus for each wavelength scan, because the focal length of a zone plate varies as a function of wavelength; remaining focus discrepancies for each wavelength and zone plate can then be removed in the alignment procedure. For both ZPC and hZPC, the feature being considered is a 560nm (mask pitch) 3:1 line-space in the horizontal (shadowing) orientation.

3. Computational Methods

3.1 Phase retrieval

We perform phase retrieval independently for each wavelength, and for each we recover the complex diffraction orders contained within the image. The algorithm is more thoroughly laid out in the Appendix. In short, for a given wavelength it takes as inputs the measured ZPC images, as well as the intensity of each scattered order, measured with

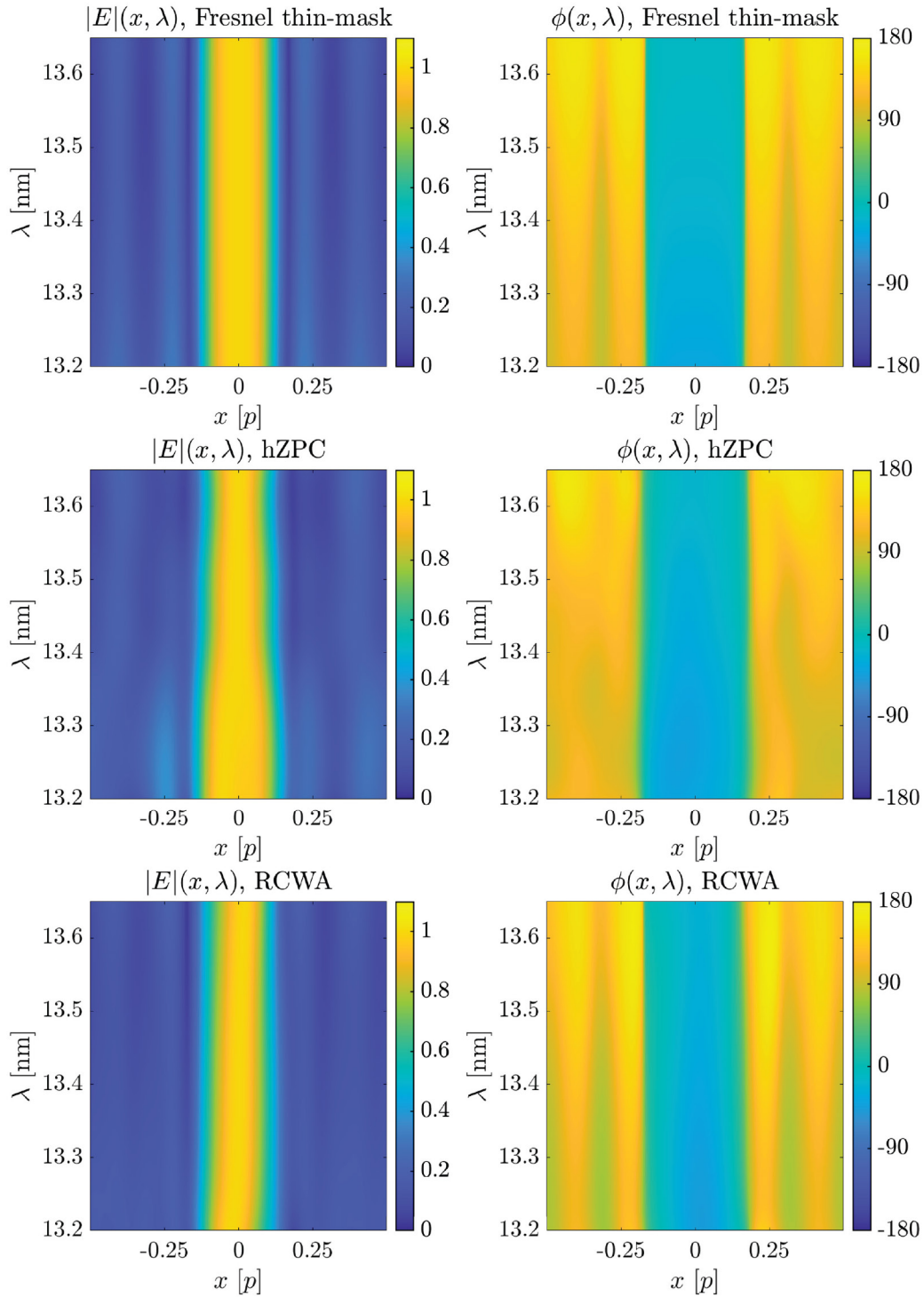


Figure 6. $E(\lambda, 0)$ Electric field as a function of wavelength and position, for Fresnel thin-mask, hZPC, and RCWA. All three show similar trends in how the phase increases with increasing wavelength, but the trends in the amplitude are fairly different, with hZPC showing a broadening of the central peak at low wavelengths, whereas RCWA shows the peak shifting to the left but with roughly constant width.

scatterometry; the scatterometry data is not strictly necessary, but can help improve accuracy.⁵

Then it uses the measured ZPC and scatterometry data, as well as several loosely enforced prior assumptions about the pattern, to reconstruct the complex field. The prior assumptions used are: low-rank autocorrela-

tion (PhaseLift);⁸ binary, in-focus pattern; square-wave (possibly out of focus); minimum energy, weighted to promote low spatial frequencies. These priors are not strictly enforced, but rather serve to “nudge” the solution in the right direction while remaining consistent with the data.

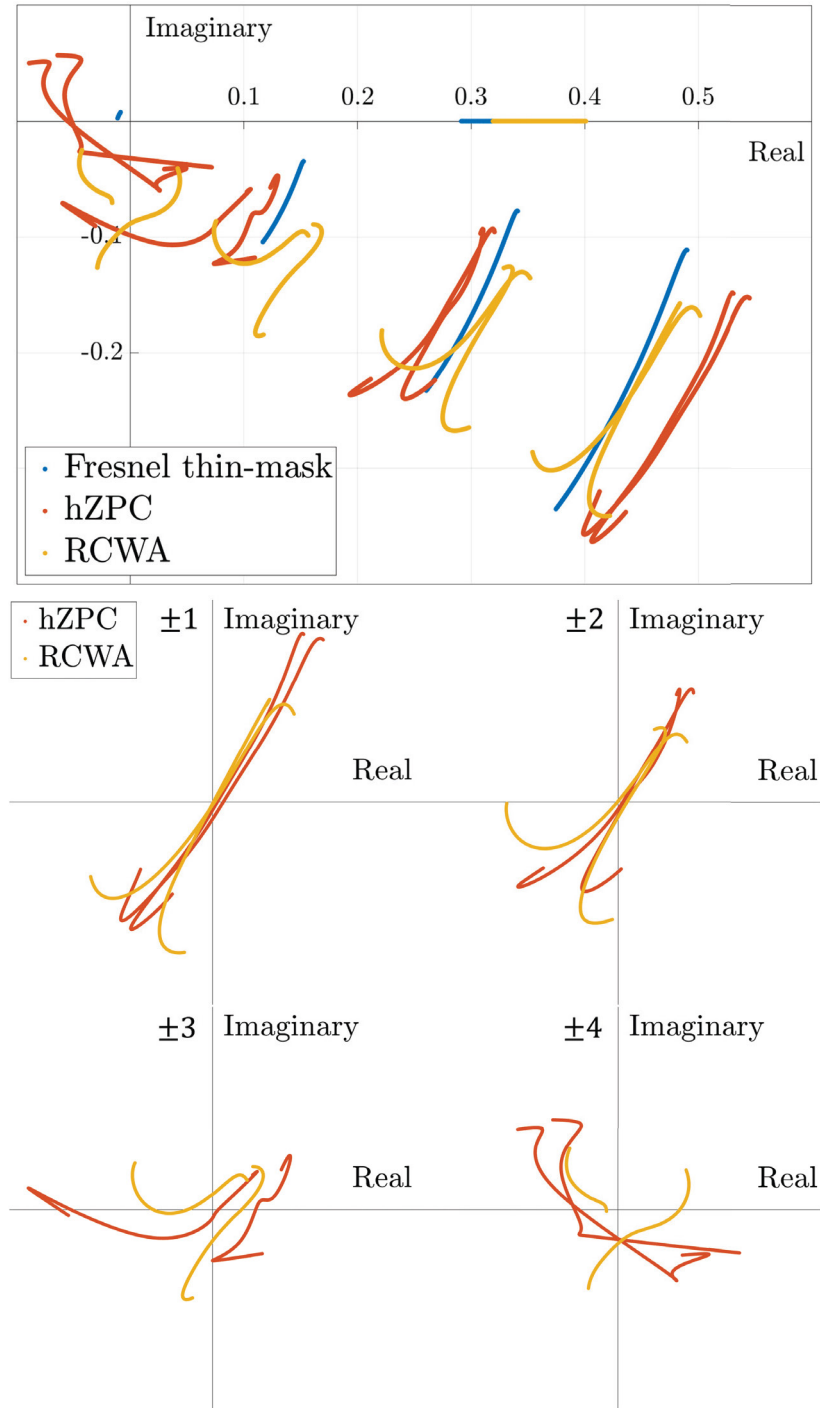


Figure 7. Complex plane Scattered orders plotted in the complex plane for Fresnel thin-mask, hZPC, and RCWA. Both hZPC and RCWA have asymmetric $\pm m$ orders characteristic of shadowing, particularly in how the asymmetry increases for higher order diffraction due to increased divergence of the diffraction angles. They also both display curvature, with opposite curvature for + and - orders. Although the orders are shifted in hZPC relative to RCWA, after they have been aligned in the bottom plots, the similarities in these hyperspectral diffraction trends become more apparent.

3.2 Generating roughness-free model

An entirely different computational routine is also necessary to transfer the film model recovered from reflectometry into one that can be used in rigorous coupled-wave analysis (RCWA). The key stumbling block is that the reflectometry model uses the physical parameters of thickness, roughness, and complex refractive index to calculate the Fresnel reflec-

tance, whereas the geometry in RCWA does not include roughness and instead assumes perfectly flat interfaces. An obvious but ultimately naive approach to solving the issue is to simply remove surface roughness from the reflectometry model; but unfortunately this results in substantial phase errors, shown in Figure 4 (top, blue curve vs red curve). This is a crucial effect to understand for designing EUV absorbers, particularly

for an attenuated phase shift mask (aPSM), where the current state of the art is reliant on using rigorous calculations such as RCWA¹⁻⁴ which presumably do not include roughness, possibly calling into question exactly how accurately these simulations would compare with an actual photomask that does contain roughness.

Our current solution for removing roughness from the model is to take the reflectometry film model, and iteratively reduce the roughness, while enforcing that the Fresnel reflectance, including phase, changes by as little as possible. As shown in Figure 4, the optimized curve (yellow) is much closer to the original Fresnel coefficient (blue) compared to the “naive” approach (red). This greatly improved consistency between RCWA and reflectometry allows us to at least qualitatively compare results from RCWA, the Fresnel thin-mask model, and the hZPC experiment.

At the same time there is still some residual error, which suggests that even this approach may be limited in how well the idealized roughness-free geometry can truly predict 3D scattering. Furthermore, other idealizations are also present in the simulation geometry such as assuming an idealized vertical etch. All this is to say that while rigorous simulations may in some sense be the gold standard for predicting mask 3D effects, their predictions should be taken with a grain of salt, hence the need to measure 3D effects experimentally.

4. Results and Discussion

In this section we present three different complex fields: the first is the Fresnel thin-mask using the reflectometry model, the second is the reconstruction from the hZPC experiment, and the third is the output of RCWA using the optimized roughness-free reflectometry model. In Figure 5 we present the 1D reconstructed electric field of one period of the grating for the three cases, at the nominal wavelength of $\lambda = 13.5\text{nm}$, and a 6° illumination angle. Note that while the nominal duty cycle is 25%, we used a slightly different value of 25.5% in an attempt to match the experimental CD from ZPC. Both ZPC and RCWA deviate from the Fresnel thin-mask; both are asymmetric, for example in the main peak both show a higher intensity on the left side than the right. But for ZPC the main peak appears to be split into two peaks, whereas for RCWA there is still just one peak, but it is narrower than for the Fresnel thin-mask. Both ZPC and RCWA also display a tilted phase in the main peak; but whereas the ZPC result shows the phase tilting slightly up and to the left throughout the entire peak, the RCWA result displays a transition from a downward to an upward tilt. There are potential confounding factors for both RCWA and ZPC in terms of determining which is more accurate. On the one hand the RCWA simulation is only an idealized geometry, with no surface roughness and a vertical etch. On the other hand the ZPC reconstruction could potentially suffer from experimental errors, with the most probable errors arising either from lateral misalignment or focus error. But in either case, the curves clearly show the difficulty of characterizing mask 3D effects, either in simulation or experiment. Furthermore, this is a relative “large” pitch at 560nm (mask scale). In the horizontal (shadowing) orientation, this would correspond to 140nm or 70nm on the wafer scale, or a $k_1 = \frac{p}{2\lambda} \text{NA}$ of 1.7 and 1.4 for 0.33 and 0.55 NA respectively. That is to say this feature is $6\text{--}7 \times$ larger than the minimum possible value of $k_1 = 0.25$, so 3D effects will be much greater for critical features near the resolution limit.

With the extension to hZPC, we can view how the complex field varies not only in space, but also in wavelength. Figure 6 shows an image of the electric field as a function of wavelength and position for Fresnel thin-mask, hZPC, and RCWA. All three show similar trends, for instance increasing phase with increasing wavelength in the absorber region. But there are also clear differences, such as the trends in the amplitude of the central peak. The peak broadens for hZPC at low wavelengths, whereas the peak width stays approximately constant but shifts to the left for RCWA at low wavelengths. We can gain some additional intuition about the hyperspectral trends in the diffraction pattern by viewing the scattered orders in the complex plane, shown in Figure 7. The top plot displays the complex diffraction orders vs wavelength for all 3 curves; we can see that whereas the Fresnel thin-mask model has symmetric $\pm m$ orders which form arcs in the complex plane (due to the changing Fresnel reflectance), both RCWA and hZPC have asymmetric $\pm m$ diffraction orders. We can more clearly compare these trends in the bottom 4 plots that show the $\pm m$ orders for just RCWA and hZPC, with the mean removed to approximately align them. We see an interesting curvature of the orders, with opposite curvature for + and - orders, particularly in the ± 1 and ± 2 orders. The asymmetry between the orders continually

increases as m increases (excluding ± 4 for hZPC, which are likely not very accurate due to their relatively low magnitude and the susceptibility of high spatial frequencies to defocus error). This kind of trend where $\pm m$ asymmetry increases for increasing m is a characteristic mask 3D effect associated with shadowing; one way to interpret why this should happen intuitively is that as m increases, the angular divergence between the $\pm m$ orders increases, and due to the offset chief ray in this orientation, one order gets closer to normal incidence and the other gets more oblique. Therefore the $\pm m$ orders experience very different 3D scattering because of their divergent propagation angles.

5. Conclusion

We have demonstrated an extension of previous work on using Zernike Phase Contrast (ZPC) for making a spatially resolved measurement of the complex electric field scattered from an EUV mask. Our extension is to make the ZPC measurement at multiple wavelengths, hence the name hyperspectral Zernike Phase Contrast (hZPC). Directly measuring the complex electric field is a problem of great importance for achieving the highest possible image quality in the presence of mask 3D effects. By adding the additional capabilities of measuring at multiple illumination wavelengths, we open up the possibility of empirically measuring a higher dimensional description of scattering, which would most generally include two spatial dimensions and three illumination dimensions, but in this first demonstration of the approach we only include one spatial dimension (due to the one dimensional pattern) and one illumination dimension (wavelength). Traditionally the complex field scattered from a certain illumination plane wave has been accessible only through simulations such as rigorous coupled wave analysis (RCWA), but now ZPC and hZPC open up the possibility of empirically verifying or calibrating these rigorous simulations. We also present the challenge of constructing an accurate model for RCWA, due to surface roughness which is not captured in the idealized RCWA geometry. Our physical model of the absorber and multilayer was determined by reflectometry, and unfortunately includes interface roughness. We show that simply setting roughness to zero results in a large phase error and therefore RCWA would not produce an accurate estimate of the phase. We get around this issue by constructing a roughness-free model where we adjust other physical parameters to make the Fresnel reflection coefficients of absorber and multilayer as close as possible to the original model. Using this roughness free model for RCWA, we are able to compare the complex electric fields from the Fresnel thin-mask model, hZPC, and RCWA. There are noticeable differences between hZPC and RCWA but both deviate from the Fresnel thin-mask model, and furthermore the deviations in both cases are qualitatively similar when looking at the hyperspectral diffraction pattern in the complex plane. Both hZPC and RCWA display 3D effects characteristic of shadowing, such as asymmetry between the $\pm m$ diffraction orders which grows larger with increasing m . Furthermore, the $+m$ and $-m$ orders both deviate from the symmetric arcs predicted by the Fresnel thin-mask model, and the deviation takes on opposite curvature for $+m$ and $-m$ orders. We hope the newfound ability to measure arbitrary complex fields scattered from different plane-wave illumination conditions may open up new possibilities for measuring and understanding mask 3D effects, allowing experimental measurement of effects that were previously accessible only through simulation.

6. Acknowledgments

This research is sponsored by Intel Corporation.

This work was performed in part at Lawrence Berkeley National Laboratory which is operated under the auspices of the Director, Office of Science, of the U.S. Department of Energy under Contract No. DE-AC02-05CH11231.

7. References

- [1] M.-C. van Lare, F. J. Timmermans, and J. Finders, “Alternative reticles for low- k_1 euv imaging,” in *International Conference on Extreme Ultraviolet Lithography 2019*, **11147**, p. 111470D, International Society for Optics and Photonics, 2019.
- [2] H. Song, L. Zavyalova, I. Su, J. Shiely, and T. Schmoeller, “Shadowing effect modeling and compensation for euv lithography,” in *Extreme Ultraviolet (EUV) Lithography II*, **7969**, p. 796910, International Society for Optics and Photonics, 2011.

- [3] O. Wood II, K. Wong, V. Parks, P. Kearney, J. Meyer-Illse, V. Luong, V. Philipsen, M. Faheem, Y. Liang, A. Kumar, et al., "Improved ru/si multilayer reflective coatings for advanced extreme-ultraviolet lithography photomasks," in *Extreme Ultraviolet (EUV) Lithography VII*, **9776**, p. 977619, International Society for Optics and Photonics, 2016.
- [4] S. Sherwin, L. Waller, A. Neureuther, and P. Naulleau, "Advanced multilayer mirror design to mitigate euv shadowing," in *Extreme Ultraviolet (EUV) Lithography X*, **10957**, p. 1095715, International Society for Optics and Photonics, 2019.
- [5] S. Sherwin, I. Cordova, R. Miyakawa, L. Waller, A. Neureuther, and P. Naulleau, "Quantitative phase retrieval for euv photomasks," in *Extreme Ultraviolet (EUV) Lithography XI*, **11323**, p. 1132315, International Society for Optics and Photonics, 2020.
- [6] S. Sherwin, I. Cordova, R. Miyakawa, M. Benk, L. Waller, A. Neureuther, and P. Naulleau, "Picometer sensitivity metrology for euv absorber phase," in *Extreme Ultraviolet Lithography 2020*, **11517**, p. 1151707, International Society for Optics and Photonics, 2020.
- [7] C. Mack, *Fundamental principles of optical lithography: the science of microfabrication*, John Wiley & Sons, 2008.
- [8] E. J. Candes, T. Strohmer, and V. Voroninski, "Phaselift: Exact and stable signal recovery from magnitude measurements via convex programming," *Communications on Pure and Applied Mathematics* **66**(8), pp. 1241-1274, 2013.
- [9] S. Boyd, S. P. Boyd, and L. Vandenberghe, *Convex Optimization*, Cambridge University Press, 2004.
- [10] J. Wright and Y. Ma, *High-Dimensional Data Analysis with Low-Dimensional Models: Principles, Computation, and Applications*, Cambridge University Press, 2021.

5. APPENDIX

5.1 Phase retrieval algorithm

The algorithm is primarily based on the PhaseLift algorithm for convex phase retrieval, wherein one does not directly solve for the complex field \tilde{E} , but instead for its autocorrelation $\mathbf{X} = \tilde{E} \tilde{E}^*$, where $\tilde{E} \in \mathbb{C}^n$ is an $n \times 1$ vector of Fourier coefficients, and $\mathbf{X} \in \mathbb{C}^{n \times n}$ is an $n \times n$ positive semi-definite autocorrelation matrix.⁸ This is advantageous because the image intensity is linear in \mathbf{X} whereas it is nonlinear (quadratic) in \tilde{E} . We call this linear operator $\mathcal{L} : \mathbf{X} \in \mathbb{C}^{n \times n} \mapsto I \in \mathbb{R}^M$, which takes in an $n \times n$ autocorrelation matrix \mathbf{X} and outputs a vector of M intensity values I (where M is the number of pixels per image times the number of images). We can also express \mathcal{L} in terms of its matrix representation $\mathbf{L} \in \mathbb{C}^{n^2 \times M}$, such that $\mathbf{L}[\mathbf{X}]_{n^2 \times 1} = \mathcal{L}(\mathbf{X})$, where the $[\cdot]_{n^2 \times 1}$ denotes reshaping to size $n_1 \times n_2$. Switching to a linear imaging model makes the least-squares inverse problem convex, whereas nonlinear least-squares is generally non-convex. Practically, a convex problem offers mathematical guarantees about convergence to a true solution from any initial guess, whereas a non-convex problem does not.⁹

But the switch to this linear formulation does unfortunately increase the dimension of the unknown variable from n to n^2 without any additional measurements. This is mitigated by placing a low-rank constraint on \mathbf{X} , because the true $\mathbf{X} = \tilde{E} \tilde{E}^*$ is the outer-product of two vectors and therefore rank-1. Rank-1 matrices are extremely "rare" in $\mathbb{C}^{n \times n}$,¹⁰ so this approach essentially reduces the dimension of the problem, without making any prior assumptions on which dimensions to remove. While the rank function is not convex, a low-rank solution is promoted by minimizing the trace of \mathbf{X} , which is equivalent to the sum of singular values for a positive semi-definite matrix like \mathbf{X} . The sum of singular values is also called the nuclear norm of a matrix (denoted $\|\cdot\|_*$), and it is the so-called convex relaxation (or best convex approximation) of the rank of a matrix.⁹ The nuclear norm, although not always differentiable, can be minimized with a proximal operator that applies a soft threshold to the singular values of a matrix while maintaining the same singular vectors. Concretely, if $\mathbf{U}\Sigma\mathbf{V}^* = \mathbf{X}$ is the singular value decomposition of \mathbf{X} , then $\text{prox}_{\alpha}(\mathbf{X}) = \mathbf{U} \max\{0, \Sigma - \alpha\mathbf{I}\} \mathbf{V}^*$.¹⁰ This intuitively reduces the rank of the matrix by setting singular

values below α to 0 (and reducing the magnitude of the rest by α). We write the basic PhaseLift problem as:⁸

$$\min_{\mathbf{X} \in \mathbb{C}_+^{n \times n}} \|\mathbf{I} - \mathbf{L}[\mathbf{X}]\|_2^2 + \alpha_1 \|\mathbf{X}\|_*$$

We augment the problem in a few additional ways: data consistency with scatterometry measurements of the diffraction intensities, closeness to a subspace of (defocused) thin-mask scattering functions, and closeness of the nonzero diffraction orders to forming a straight line in the complex plane, and attenuated high-frequency content.

The scatterometry measurements allow us to constrain the amplitude of \mathbf{X} . We take the diffraction orders measured by scatterometry, $|\tilde{E}_s|$, and calculate the outer product $|\mathbf{X}_0| = |\tilde{E}_s| |\tilde{E}_s|^*$; we can then penalize the deviation of $|\mathbf{X}|$ from $|\mathbf{X}_0|$ by minimizing the norm of the distance, where in this case we use the Frobenius norm-squared:

$$\|\mathbf{X} - |\mathbf{X}_0|\|_F^2 = \|\mathbf{X} - |\mathbf{X}_0|\|_{n^2 \times 1}^2$$

The use of an amplitude constraint unfortunately breaks the convexity of the problem, but previous simulations have shown that using scatterometry data in this way can greatly improve accuracy.⁵

The subspace of thin-mask scattering functions is determined by the span of a dictionary which can be rapidly generated on the fly from a given range of parameters. Say we have a matrix $\mathbf{P} \in \mathbb{R}^{d \times N}$ of N designs, each with d parameters. In our case the parameters are the duty cycle, amplitude, phase, and defocus, representing our assumption that the final function is approximately a square wave (possibly out of focus). We define the Fresnel thin-mask scattering function $f_s(x) : x \in \mathbb{R}^d \mapsto E \in \mathbb{C}^n$, which takes in a vector of d parameters (x) and returns a set of n complex diffraction orders (E). Then we compute our dictionary $\mathbf{D} \in \mathbb{C}^{n^2 \times N}$, where column j is the (vectorized) autocorrelation matrix $\mathbf{D}_{(j,:)} = [fs(\mathbf{P}_{(j,:)}) fs(\mathbf{P}_{(j,:)})^*]_{n^2 \times 1}$. We then compute a projection matrix onto the range of \mathbf{D} by means of the SVD. If $\mathbf{U}\Sigma\mathbf{V}^* = \mathbf{D}$ is the (possibly truncated) SVD of \mathbf{D} , then the projection matrix is $\mathbf{P}_D = \mathbf{U}\mathbf{U}^*$. Finally we can enforce that our solution be close to the range of the subspace by minimizing:

$$\|\mathbf{X}\|_{n^2 \times 1} - \mathbf{P}_D \mathbf{X}\|_{n^2 \times 1}^2$$

This constraint is convex, because it is the composition of a norm and a linear map, both of which are convex.⁹

The straight line constraint is essentially another kind of binary constraint, but the implementation is quite different. The intuition behind this constraint is that for any even binary function, the nonzero Fourier coefficients lie on a straight line in the complex plane. For example, a square-wave impulse function centered on the origin has purely real Fourier coefficients. So we attempt to enforce this constraint on each column of \mathbf{X} (because each column of \mathbf{X} should be a scaled copy of \tilde{E} , which should follow this straight-line rule). For column j , we first define an $n-1 \times 2$ real-valued matrix $\mathbf{A}(\mathbf{X}_{(j,:)})$ which contains all the nonzero diffraction orders of $\mathbf{X}_{(j,:)}$, with the two columns containing the real and imaginary components respectively. Concretely, $\mathbf{A}(\mathbf{X}_{(j,:)}) = [\text{Re}\{\mathbf{X}_{(j,m \neq 0)}\}, \text{Im}\{\mathbf{X}_{(j,m \neq 0)}\}] \in \mathbb{R}^{n-1 \times 2}$. A straight line in 2D space would be described by a rank-1 matrix. As before we take the convex relaxation of rank as the nuclear norm. Then we enforce this constraint by minimizing:

$$\sum_j \|\text{Re}\{\mathbf{X}_{(j,m \neq 0)}\} \|\text{Im}\{\mathbf{X}_{(j,m \neq 0)}\}\|_* = \sum_j \|\mathbf{A}(\mathbf{X}_{(j,:)})\|_*$$

As before with \mathbf{X} we can apply a soft threshold to the singular values of $\mathbf{A}(\mathbf{X}_{(j,:)})$ to enforce this constraint, and then use the result to update the nonzero diffraction orders of $\mathbf{X}_{(j,:)}$. This operation is also convex, because this amounts to the nuclear norm composed with a linear map.

The final constraint is to favor low-frequency over high-frequency content, because the high spatial frequencies will be most strongly impacted by focus errors while at the same time their relatively lower magnitude makes them more susceptible to experimental errors. We accomplish this with a simple minimum-energy constraint, with a weighting factor that more heavily penalizes high frequencies. We define an $n \times 1$ weighting

vector $w = e^{-f^2/2\sigma^2}$, where f is the spatial frequency and σ is a Gaussian standard deviation. Then the outer product of this vector, $\mathbf{W} = ww^* \in \mathbf{R}_+^{n \times n}$, can serve as a low-pass weighting matrix for \mathbf{X} . So to minimize the high frequencies, we minimize:

$$\|\mathbf{X}\|_{n^2 \times 1} - \text{diag}[\mathbf{W}][\mathbf{X}]_{n^2 \times 1}\|_2^2$$

This can be minimized by simply scaling each element of \mathbf{X} by a factor proportional to the corresponding element of \mathbf{W} .

The total optimization can then be written as:

$$\min_{\mathbf{X} \in \mathbf{C}_+^{n \times n}}$$

$$\|\mathbf{I} - \mathbf{L}[\mathbf{X}]\|_{n^2 \times 1}\|_2^2$$

$$+ \alpha_1 \|\mathbf{X}\|_*$$

$$+ \alpha_2 \|[\mathbf{X}] - [\mathbf{X}_0]\|_{n^2 \times 1}\|_2^2$$

$$+ \alpha_3 \|\mathbf{X}\|_{n^2 \times 1} - \mathcal{P}_{\mathbf{D}}[\mathbf{X}]_{n^2 \times 1}\|_2^2$$

$$+ \alpha_4 \sum_j \|\mathcal{A}(\mathbf{X}_{(j,:)})\|_*$$

$$+ \alpha_5 \|\mathbf{X}\|_{n^2 \times 1} - \text{diag}[\mathbf{W}][\mathbf{X}]_{n^2 \times 1}\|_2^2$$

Solve for positive semidefinite \mathbf{X}

Imaging data consistency

Low-rank \mathbf{X}

Scatterometry data consistency

Distance from dictionary (defocused thin-mask)

Low-rank $\mathcal{A}(\mathbf{X}_{(j,:)})$ (in-focus binary object)

Penalize high spatial frequencies



Sponsorship Opportunities

Sign up now for the best sponsorship opportunities

Photomask Technology + EUV Lithography 2022 Digital Forum

Contact: Melissa Valum

Tel: +1 360 685 5596; melissav@spie.org

Advanced Lithography + Patterning 2022

Contact: Teresa Roles-Meier

Tel: +1 360 685 5445; teresar@spie.org

Advertise in the BACUS News!

The BACUS Newsletter is the premier publication serving the photomask industry. For information on how to advertise, contact:

Melissa Valum
Tel: +1 360 685 5596
melissav@spie.org

BACUS Corporate Members

Acuphase Inc.
American Coating Technologies LLC
AMETEK Precitech, Inc.
Berliner Glas KGaA Herbert Kubatz GmbH & Co.
FUJIFILM Electronic Materials U.S.A., Inc.
Gudeng Precision Industrial Co., Ltd.
Halocarbon Products
HamaTech APE GmbH & Co. KG
Hitachi High Technologies America, Inc.
JEOL USA Inc.
Mentor Graphics Corp.
Molecular Imprints, Inc.
Panavision Federal Systems, LLC
Profilocolore Srl
Raytheon ELCAN Optical Technologies
XYALIS

Industry Briefs

■ Global Fab Equipment Spending Projected to Reach New High of Nearly \$100 Billion in 2022

Michael Hall and Christian G. Dieseldorff, www.semi.org

Powered by digital transformation and other secular technology trends, global semiconductor equipment investments for front end fabs in 2022 are expected to reach nearly US\$100 billion to meet soaring demand for electronics after topping a projected \$90 billion this year, both new records.

The new fab equipment spending records will mark a rare three consecutive years of growth that began in 2020, bucking the historical cyclical trend of a one- or two-year expansion followed by a year or two of tepid growth or declines. The semiconductor industry last saw more than two consecutive years of growth in the mid-1990s.

<https://www.semi.org/en/news-media-press/semi-press-releases/global-fab-equipment-spending-to-reach-new-high-of-nearly-%24100-billion-semi-reports>

■ TSMC's Second Gen EUV 3nm Process Can Reduce Layers By 20% & Improve Gross Margin

Ramish Zafar, www.wccftech.com

According to a report from Citigroup, the Taiwan Semiconductor Manufacturing Company (TSMC) is geared up for successive monthly revenue growth, removing the seasonality aspect of its business alongside significant cost reduction through the second generation of its leading-edge 3-nanometer process. TSMC is responsible for manufacturing semiconductors for Apple Inc., NVIDIA, Qualcomm. The company's successful partnership with Advanced Micro Devices, Inc (AMD) is also playing a crucial role in the latter's meteoric rise in the computing industry.

<https://wccftech.com/tsmcs-second-gen-euv-3nm-process-can-reduce-layers-by-20-improve-gross-margin/>

■ Optimizing VSB Shot Count for Curvilinear Masks

Jan Willis, www.semiengineering.com

The increased photomask write time with a variable-shape e-beam (VSB) writer has been a barrier to the adoption of inverse lithography technology (ILT) beyond the limited usage for hot spots. The collaborative study between Micron Technology and D2S to optimize VSB shot count for curvilinear masks was to find the most efficient way to reduce the VSB write time for curvilinear photomasks without losing the benefit of improved wafer performance. Blindly optimizing the VSB mask writer shot count (a proxy for the write time) won't result in the same wafer performance benefits. The proposal is to co-optimize the shot count reduction with the ILT algorithm using mask and wafer simulation (MWCO). The wafer performance from MWCO is comparable to the full curvilinear ILT written on multi-beam writers. MWCO is not suitable for EUV masks, however, because of the larger geometry count and the higher energy required to expose the slower resists to achieve the required precision.

<https://semiengineering.com/optimizing-vsbs-shot-count-for-curvilinear-masks/>

■ Chip Supply to Stay Tight for Another Year: Toshiba

Bloomberg, www.taipeitimes.com

Toshiba Corp said it would not be able to meet demand for power-regulating chips for another year and, in certain cases, through the end of next year, offering a fresh warning for makers of vehicles, consumer electronics and industrial machines struggling with component shortages.

"The supply of chips will remain very tight until at least September next year," said Takeshi Kamebuchi, a director in charge of semiconductors. "In some cases, we may find some customers not being fully served until 2023."

Material shortages and demand outpacing output capacity are to blame for Toshiba's inability to fulfill orders for a component that does not require advanced production technology and has typically been deemed a commodity, Kamebuchi said.

<https://www.taipeitimes.com/News/biz/archives/2021/09/04/2003763750>

Join the premier professional organization for mask makers and mask users!

About the BACUS Group

Founded in 1980 by a group of chrome blank users wanting a single voice to interact with suppliers, BACUS has grown to become the largest and most widely known forum for the exchange of technical information of interest to photomask and reticle makers. BACUS joined SPIE in January of 1991 to expand the exchange of information with mask makers around the world.

The group sponsors an informative monthly meeting and newsletter, BACUS News. The BACUS annual Photomask Technology Symposium covers photomask technology, photomask processes, lithography, materials and resists, phase shift masks, inspection and repair, metrology, and quality and manufacturing management.

Individual Membership Benefits include:

- Subscription to BACUS News (monthly)
- Eligibility to hold office on BACUS Steering Committee

spie.org/bacushome

Corporate Membership Benefits include:

- 3-10 Voting Members in the SPIE General Membership, depending on tier level
- Subscription to BACUS News (monthly)
- One online SPIE Journal Subscription
- Listed as a Corporate Member in the BACUS Monthly Newsletter

spie.org/bacushome

C A L E N D A R

2022



SPIE Advanced Lithography

27 February - 3 March 2022
San Jose Convention Center
San Jose, California, USA
www.spie.org/al



Photomask Japan

25-27 April 2022
PACIFICO Yokohama
Yokohama, Kanagawa, Japan
www.photomask-japan.org



EMLC 2022

20-23 June
Leuven, Belgium

SPIE is the international society for optics and photonics, an educational not-for-profit organization founded in 1955 to advance light-based science, engineering, and technology. The Society serves more than 255,000 constituents from 183 countries, offering conferences and their published proceedings, continuing education, books, journals, and the SPIE Digital Library. In 2020, SPIE provided over \$5 million in community support including scholarships and awards, outreach and advocacy programs, travel grants, public policy, and educational resources. spie.org

SPIE.

International Headquarters
P.O. Box 10, Bellingham, WA 98227-0010 USA
Tel: +1 360 676 3290
Fax: +1 360 647 1445
help@spie.org • spie.org

Shipping Address
1000 20th St., Bellingham, WA 98225-6705 USA

Managed by SPIE Europe

2 Alexandra Gate, Ffordd Pengam, Cardiff,
CF24 2SA, UK
Tel: +44 29 2089 4747
Fax: +44 29 2089 4750
spieurope@spieurope.org • spieurope.org

You are invited to submit events of interest for this calendar. Please send to lindad@spie.org.